

NOAA-20 VIIRS Reflective Solar Band Post-launch Calibration Updates Two Years In-orbit

Taeyoung Choi, Changyong Cao, Slawomir Blonski, Wenhui Wang, Sirish Uprety, Xi Shao

Abstract—The NOAA-20 Visible Infrared Imaging Radiometer Suite (VIIRS) was launched on November 18, 2017, and it has been operational for more than two years and follows the first Joint Polar Satellite System (JPSS) series of the Suomi National Polar-Orbiting Partnership (S-NPP) mission. VIIRS has 14 Reflective Solar Bands (RSBs) covering a spectral range of 0.41 to 2.3 μ m. The primary source of RSB calibration is the Solar Diffuser (SD) and time dependent SD degradation is monitored by the Solar Diffuser Stability Monitor (SDSM). The initial instability of the SD degradation (H-factor) was resolved by updating SDSM Sun screen transmittance function combining yaw maneuver data and on-orbit SDSM data sets. After the H-factor improvements, the VIIRS RSB calibration coefficients (F-factors) are updated and applied to the operational Sensor Data Record (SDR) product generation. To validate the SD F-factors, the lunar F-factors are calculated by using a lunar irradiance model and compared the trend differences between them. Over the two years of operation, decreasing trends have been calculated with the SD F-factors, whereas constant lunar F-factors were observed in bands M1 to M4. With these discrepancies, the operational F-factors remained unchanged since April 2018 because the Deep Convective Cloud (DCC) and cross-calibration comparison results didn't show any further degradations in these bands. All the possible radiometric calibration sources such as SD and lunar F-factors, DCC trends, and cross calibration results are monitored, compared, and applied by NOAA VIIRS sensor data record science team for the best quality of the VIIRS SDR product.

Index Terms—NOAA-20, VIIRS, RSB, SD, SDSM, SD degradation, H-factor, F-Factor, radiometric calibration, Lunar irradiance model, SDR, DCC, Cross Calibration

I. INTRODUCTION

THE National Oceanic and Atmospheric Administration (NOAA)-20 Visible Infrared Imaging Radiometer Suite (VIIRS) is a major NOAA's earth observing polar orbiting sensors following the predecessor Suomi National Polar-Orbiting Partnership (S-NPP) satellite mission under the Joint Polar Satellite System (JPSS) program. It was launched on November 18, 2017 in a sun-synchronous polar orbit with an equator crossing time of 13:25 in ascending node and a nominal altitude of 829 km providing earth observations of land, ocean and atmosphere for short-term and long-term monitoring and forecasting. Similar to S-NPP, NOAA-20 also carries other

state-of-art instruments called the Advanced Technology Microwave Sounder (ATMS), the Cross-track Infrared Sounder (CrIS), and the Ozone Mapping and Profiler Suite Nadir (OMPS). NOAA-20 VIIRS provides a complete global observation daily with a large scan angle of 112 degrees with the 22 spectral band covering 0.41 μ m to 12.5 μ m with spatial resolution of 750 and 350 meters for Moderate (M) resolution and Imaging (I) bands [2-5]. Because of the daily entire earth coverage per day, the VIIRS Sensor Data Record (SDR) products have provided many environmental and weather related products called Environmental Data Records (EDRs) such as aerosol, cloud, fire, polar wind, sea surface temperature, snow, vegetation fraction, etc. The detailed EDR product catalogue and documentations can be found at https://www.star.nesdis.noaa.gov/jpss/JPSS_products.php.

A series of Post Launch Tests (PLTs) had been performed to check how the VIIRS SDR products were performing within the JPSS program level 1 Requirements. For RSBs, the calibration uncertainty in spectral reflectance for a scene at a typical radiance is expected to be less than 2%, which had been demonstrated in pre-launch laboratory testing [2]. With this radiometric requirement, it was necessary to check on-orbit behavior and performance of the primary RSB radiometric calibration source of SD and SDSM for its degradation monitoring. For S-NPP VIIRS, it was found that there were differences between the prelaunch and yaw maneuver derived SD and SDSM related transmittance functions. The transmittance function that were derived from the yaw maneuver data significantly improved SD degradation and calibration coefficients called F-factors [6, 7]. Similar to the S-NPP case, NOAA-20 VIIRS also showed significant differences in the transmittance function especially for the SDSM Sun view screen transmittance function [1, 8]. There were large initial SD degradation (i.e. H-factor) up to 1.6% in all the 8 detectors because of the problems in the prelaunch Look-Up Table of the SDSM Sun view screen transmittance [9]. The operational version of H and F-factors were derived by adding regular on-orbit SDSM data sets with time dependent gain change correction in the SDSM detectors 6, 7, and 8 [9].

After the initial update of the screen transmittance and SD bidirectional reflectance functions, the H and F-factors showed very consistent trending results [9]. In early 2019, these

functions were updated again after covering the whole operational range of the solar azimuth angle. Once the primary SD F-factors show reasonable trends, they were compared with the lunar F-factors to validate the long-term detector gain changes. There were SD and lunar F-factor differences observed especially in the short wavelength bands. The SD F-factors indicated inverse detector gain degradation (or gain increase) over time when they were compared to the lunar F-factors considering the annual oscillation pattern. To validate these changes, the DCC trending and cross-calibration results were checked to track the real detector gain changes. From the SD F-factors, lunar F-factors, DCC trending and cross-calibration results, the final operational RSB F-factors were decided and applied the operational version of the VIIRS SDR products produced by NOAA.

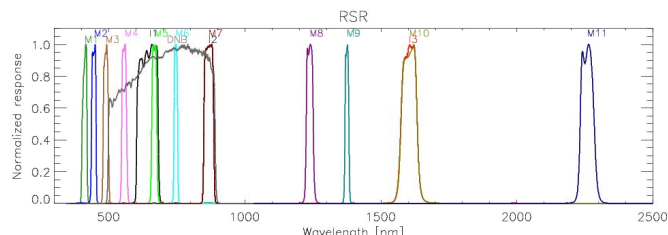


Fig. 1. NOAA-20 VIIRS Relative Spectral Response (RSR) function plot.

II. OVERVIEW OF VIIRS SENSOR

As a cross-track scanning radiometer, VIIRS sensor covers a spectral range from 410nm to 2,250nm with 3 Imaging (I) bands and 11 Moderate (M) resolution bands as shown in Fig. 1. Note that the I2/M7 and I3/M10 are spectrally similar band pairs and the Day Night Band (DNB) has a wide spectral response range from 500 to 900nm range.

Similar to the legacy sensors such as Moderate Resolution

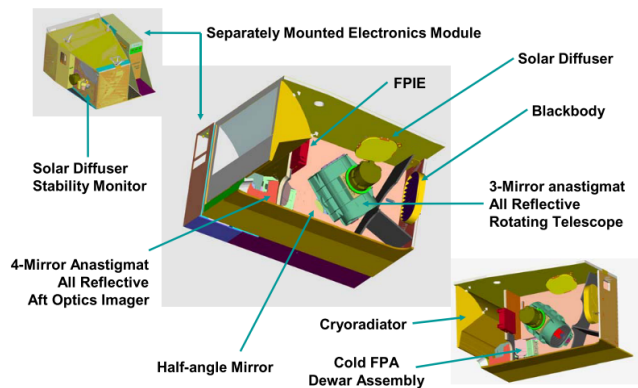


Fig. 2. Cut-out View of the VIIRS Opto-Mechanical Module [10].

Imaging Spectroradiometer (MODIS) or Very High Resolution Radiometer (AVHRR), the VIIRS sensor has similar capability of making continuous observations of the entire earth for scientific applications of atmospheric, land and ocean studies [4, 5]. For the accurate earth observations, VIIRS uses a Solar Diffuser (SD) as a primary source of the RSB radiometric calibration and the degradation of the SD is monitored by a Solar Diffuser Stability Monitor (SDSM) as shown in Fig 2

[10].

The primary on-orbit radiometric calibration of VIIRS is based on the frequent solar observations from the SD and SDSM in each orbit near the South Pole for about one minute. Within these 14 or 15 solar observations per day, the sun light is attenuated by the two SD and SDSM screens and diffusely illuminates the SD and the Spherical Integrating Sphere (SIS) in the SDSM and the Rotating Telescope Assembly (RTA) as shown in Fig 3. These SD observations are used for F-factors which is radiometric calibration coefficients that correct for the detector responsivity degradation [2, 10].

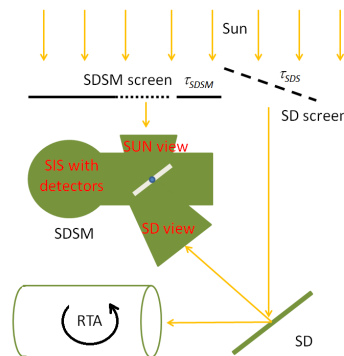


Fig. 3. A simplified diagram of SD/SDSM screens, SD, SDSM and RTA relations under the Sun illumination [1].

TABLE I
NOAA-20 VIIRS SDSM DETECTOR CENTER WAVELENGTH

| DET.# | 1 | 2 | 3 | 4 | 5 | 6 | 7 | 8 |
|--------|-------|-------|-------|-------|-------|-------|-------|-------|
| CW[NM] | 411.5 | 448.0 | 489.5 | 549.5 | 674.0 | 744.5 | 868.0 | 912.0 |

A major assumption of the on-orbit SD calibration is that the SD has the property of Lambertian surface over its degradation. The SD degradation process was modeled as the surface roughness-induce Rayleigh scattering by the Ultra Violet (UV) exposure of the sun light [11]. The time and wavelength dependent SD degradation (or called H-factor) is monitored by the SDSM that measures a relative degradation to the initial pre-launch condition as a ratioing radiometer between the Sun observations as shown in Fig 3. SDSM tracks SD degradation patterns at the SDSM detector center wavelengths as shown in Table I. The center wavelengths were calculated from the middle points of the Full Width at Half Maximum (FWHM) of the SDSM detector RSR.

The initial version of the SD degradation using the prelaunch SDSM Sun screen transmittance and SDSM Bidirectional Reflectance Function (BRF) showed abnormal large oscillations, greater than 1 percent [1]. To resolve this H-factor oscillation problem, yaw maneuver data and on-orbit SDSM data sets were used to develop new sets of SDSM SD and RTA view SD Bidirectional Reflectance Distribution Function (BRDF) with SD screen transmittance Look-Up-Tables (LUTs) and SDSM Sun screen transmittance function LUT. The newly derived H-factors significantly reduced oscillations from 0.8 percent to 0.2 percent level. After achieving stable H-factors using yaw and on-orbit SDSM data, they were applied to the VIIRS calibration equation to derive F-factors, which was also used in the NOAA’s production system called Interface Data

Processing Segment (IDPS) to generate VIIRS SDR.

III. VIIRS RADIOMETRIC CALIBRATION METHODOLOGIES

A. Primary Calibration from SD and SDSM

As shown in (1), the Earth View (EV) radiance is determined by the bias removed DN which is denoted as lower case of letter dn_{EV} , c-coefficients, and the F-factor which compensates detector changes from the SD observations. The c-coefficients were carefully determined using a National Institute of Standard and Technology (NIST) traceable light source. The band averaged c_2/c_1 showed mean value on the order of 10^{-6} for all RXB bands indicating very small non-linearity of the VIIRS detectors [12].

$$L_{EV} = \frac{F \cdot (c_0 + c_1 \cdot dn_{EV} + c_2 \cdot dn_{EV}^2)}{RVS_{EV}} \quad (1)$$

In (1), RVS_{EV} is Responses Versus Scan angle (RVS) which is scan angle dependent relative reflectivity response on the Half Angle Mirror (HAM). For the SWIR bands, a cubic equation is used to compensate non-linearity issues.

The F-factor is calculated from each SD observation as the ratio between the calculated at-aperture radiance and the measured radiance from the dn_{SD} . The F-factor is derived by

$$F_{SD} = \frac{\cos(\theta_{inc}) \cdot E_{sun} \cdot \tau_{sds} \cdot BRDF_{SDRTA} \frac{H(t)}{H_0} \cdot RVS_{SD}}{c_0 + c_1 \cdot dn_{SD} + c_2 \cdot dn_{SD}^2}. \quad (2)$$

Here, $\cos(\theta_{inc})$ is the projection effect of the sun illumination to the SD surface, E_{sun} is Earth-Sun distance corrected solar irradiance, $\tau_{sds} \cdot BRDF_{SDRTA}$ is a combined function of the SD screen vignetting function and SD BRDF at the RTA reflectance angle, $H(t)/H_0$ describes the on-orbit time-dependent SD degradation, and RVS_{SD} is the relative reflectivity of the HAM angle at the SD view. We assume that the SD is a Lambertian surface in the neighboring angles of RTA and SDSM views, so that the degradation of its surface can be modulated by the H-factor ($H(t)/H_0$) as a factor to the prelaunch measured $\tau_{sds} \cdot BRDF_{SDRTA}$ function. The H-factor is defined in following (3) as a ratio of SD and Sun view responses with the 8 SDSM detectors.

$$H = \frac{dc_{SD} \cdot \tau_{SDSM}}{dc_{sun} \cdot \cos(\theta_{SD}) \cdot \tau_{sds} \cdot BRDF_{SDSM} \cdot \Omega} \quad (3)$$

In (3), dc_{SD} is the digital count (dc) of the SD view, τ_{SDSM} is the vignetting function of the SDSM screen, dc_{sun} is the digital count (dc) of the Sun view, $\cos(\theta_{SD})$ is the projection effect of the sun illumination to the SD surface, $\tau_{sds} \cdot BRDF_{SDSM}$ is a combined function of SD BRDF at the SDSM view angle and SD vignetting function, and Ω is the solid angle effect of the SDSM SD view port. The basic idea is that the H-factor is observing the SD reflectance change by taking ratio the Sun responses as a reference from the near-simultaneous observations. Basic assumption is that the physical properties of the screen transmittance functions are temporally invariant in (3). Since the H-factor is a relative measure of SD BRDF

degradation, it is normalized to the first point, H_0 , when it is applied to the F-factor in (2).

B. Alternative Calibration using the Scheduled lunar collections

As shown in Fig. 2, the Space View (SV) port is located at the Rotating Telescope Assembly (RTA) scan angle of -65.68 degrees in the clockwise direction relative to the Earth View (EV) nadir angle. The viewing angle of the SV is about 3 degrees beyond the Earth limb at the nominal altitude of the VIIRS sensors [8]. The VIIRS sensor can observe the moon through the SV port on a monthly basis except July to October since the moon goes below the earth limb. A spacecraft roll maneuver and EV sector rotation are required to keep the moon image in the desired location of VIIRS EV frame and a near constant moon phase angle of -51 degrees [8, 13].

Similar to the SD F-factor concept, the lunar F-factor requires irradiance and observed average radiance of the moon in (4).

$$F_{moon} = \frac{I_{GIRO}}{L_{avg} \frac{\pi R_{moon}^2 (1 + \cos(\phi))}{Dist_{sat, moon}^2}} \quad (4)$$

For each RSB bands, the lunar irradiance value is provided by the Global Space-based Inter-Calibration System (GSICS) Implementation of Robotic lunar observatory (GIRO version 1.0.0), and ϕ is phase angle of the moon, R_{moon} is moon radius, and $Dist_{sat, moon}$ is distance between satellite and moon. Detailed GIRO related documentations can be found at <http://gsics.atmos.umd.edu/bin/view/Development/LunarWorkArea>. The L_{avg} represents averaged radiance of the effective lunar pixels and it is calculated by following (5).

$$L_{avg} = \frac{\sum_{Effective\ Pixels} L_{Effective\ Pixels}}{N_{Effective\ Pixels}} \quad (5)$$

Once the SD and lunar F-factors are calculated, the lunar F-factors are normalized to the SD F-factors to compare long-term trends.

C. Post production validation using DCC

Deep Convective Clouds (DCCs) are extremely cold clouds above which the absorptions due to water vapor and other gases are minimal in the visible and near infrared (VIS/NIR) spectrum. DCCs are bright targets and have nearly Lambertian reflectance. The DCC technique has been widely used for post-launch calibration and stability monitoring in the solar reflective spectrum during the past decade [14]. Monthly DCC statistics (mean and mode) have been used for S-NPP VIIRS RSB/DNB long-term calibration stability monitoring [14, 15]. Daily DCC time series were introduced at NOAA STAR since early January 2018 to support NOAA-20 VIIRS post-launch test [16, 17].

The methodology used for generating daily DCC time series is similar to that for the monthly DCCs presented in previous studies, except that the mean and mode of DCC reflectance are

TABLE II
NOAA-20 VIIRS key activities during the PLT period [1].

| Start Date | End Date | Event |
|------------|-----------|------------------------------|
| 11/18/2017 | - | N20 Launch |
| 11/29/2017 | - | VIIRS activation |
| 12/8/2017 | - | Electronics self-test |
| 12/13/2017 | - | Nadir Door Open |
| 12/30/2017 | 1/1/2018 | Instrument safe mode |
| 12/29/2017 | - | Scheduled lunar maneuver |
| 1/3/2018 | | Cryoradiator door open |
| 1/9/2018 | 1/12/2018 | Extended WUCD |
| 1/20/2018 | 1/22/2018 | Compressed WUCD |
| 1/25/2018 | 1/26/2018 | Yaw maneuvers |
| 1/27/2018 | - | Scheduled lunar maneuver |
| 2/2/2018 | 2/3/2018 | Instrument safe mode |
| 2/21/2018 | 2/23/2018 | RTA stow |
| 2/26/2018 | - | Scheduled lunar maneuver |
| 3/12/2018 | 3/14/2018 | Mid mission outgassing event |

calculated on a daily basis. The criteria for identifying VIIRS DCC pixels are summarized as follow: (1) M15 brightness temperature is less than 205 K; (2) standard deviation of TB11 of the subject pixel and eight adjacent pixels is less than 1 K; (3) standard deviation of TOA reflectance of the subject pixel and eight adjacent pixels is less than 3% relative to the mean reflectance of the nine pixels; (4) solar zenith angle is less than 40; (5) sensor view zenith angle is less than 35 [18]. The anisotropic effects in the VIS/NIR bands were corrected using the Hu et al. 2004 Angular Distribution Model (ADM). DCCs over the entire Inter-Tropical Convergence Zone (ITCZ), with latitude within $\pm 25^\circ$, were used.

D. Cross Calibration with S-NPP VIIRS with Simultaneous Nadir Overpass (SNO)

Simultaneous nadir Overpass (SNO) and extended SNO (SNOx) are two major techniques used to validate the radiometric performance of NOAA-20 VIIRS. Details on predicting SNOs for instrument comparison can be found on [19]. SNO based inter-comparison is widely used technique and is performed over high latitude polar region. During SNO event, there is an orbital intersection between two satellites and thus the instruments can be compared over near identical solar and sensor geometry which largely reduces the uncertainties due to BRDF differences. Although VIIRS instruments don't have direct SNOs, each VIIRS has SNO with Aqua MODIS and hence, each VIIRS can be compared to Aqua MODIS and the double differencing is performed to evaluate the VIIRS radiometric agreements [20]. Bias time series of each VIIRS instrument relative to Aqua MODIS is estimated. The spectral difference between the two VIIRS instrument is accounted using the (SCanning Imaging Absorption SpectroMeter for Atmospheric CHartography) SCIAMACHY spectra based Spectral Band Adjustment Factor (SBAF) (<https://satcorps.larc.nasa.gov/cgi-bin/site/showdoc?mnemonic=SBAF>). The difference between

the two bias time series provides the level of radiometric consistency between the VIIRS.

Steps:

1. VIIRS and MODIS data are collected for each SNO event
2. TOA reflectance ROI of size 30 by 30 km are extracted with center at orbital intersection for both VIIRS and MODIS
3. Compute bias, Bias= (VIIRS-MODIS)*100%/MODIS
4. Extract bias time series for both the VIIRS relative to MODIS
5. Apply SBAF to NOAA-20 VIIRS to match the S-NPP RSR equivalent reflectance
6. Analyze the difference in two bias time series to quantify the VIIRS bias

SNOs are performed over polar region whereas extended SNOs are performed over low latitude tropical region. SNOx provide comparison over wide dynamic range. Extended SNO based inter-comparison over Saharan desert and clear sky ocean has been demonstrated in the past to evaluate the radiometric performance of S-NPP VIIRS by Uprety et al. [21]. This technique is also used to quantify the NOAA-20 VIIRS bias. The steps used to compute the VIIRS bias using SNOx is similar to that of SNO. However, the comparison is performed over the overlapping region between the two instruments that are extended from the orbital intersections. Methodology details can be found in past study [21].

IV. RESULTS

A. On-orbit RSB Related Calibration Activities during the Post Launch Testing (PLT) Period

After the successful launch and activation of NOAA-20 on November 18 and 28 of 2017, SDSM started its operation in each orbit near the termination point from November 30, 2017. The On-Board Calibrator Intermediate Product (OBCIP) files include SD and SDSM collection information to derive the SD H and F-factors. The nadir door was opened on December 13, 2017 but the normal Science Data Record (SDR) product only became available from December 20, 2017 because of the lower boundary value of the VIIRS-SDR-COEFF-B-LUT in the production system. On December 29, 2017, the first scheduled lunar collection was performed but SWIR bands responses were not available since the cryoradiator door was not opened yet. After opening cryoradiator door, SWIR and Thermal Emissive Band (TEB) products were produced normally since January 3, 2018. From January 25 to 26, 2018, a series of 15 yaw maneuvers was performed to derive on-orbit version of the SD and SDSM related screen transmittance function and BRDF or BRF LUTs. The second and third scheduled lunar collection was performed on January 27 and February 26, 2018, respectively. Because of the abnormal gain degradation problems in the TEBs due to the ice buildup on the Focal Plane Assemblies (FPA), a mid-mission outgassing was suggested and performed from March 12 to 14, 2018 which restore the TEB F-factors to the nominal levels. All the NOAA-20 VIIRS related key events during the PLT period is listed in Table 2.

B. On-orbit RSB Related Calibration Activities during the Post Launch Testing (PLT) Period

After the VIIRS activation on November 29, 2017, IDPS started producing OBCIP files which includes the SD and SDSM collections data. Based on the H-factor equation (3), the initial SD degradation was calculated at each SDSM detector wavelength as shown in Fig. 4. The H-factor was normalized to the first SDSM collection point and it showed abnormal oscillation patterns of SD degradation in each detector. Considering monotonic SD degradation over time compared to the S-NPP, these oscillation patterns were caused by prelaunch measurement errors in the SDSM Sun transmittance screen LUT (τ_{SDSM} in (3)) [1]. The scattered points near day 69 when the yaw maneuvers were performed in Fig. 4 also indicated that there were problems in the prelaunch version of the SD/SDSM LUTs. To validate functionality of SD and SDSM, 15 yaw maneuvers were performed around the termination point near the South Pole. To cover beyond the operational range called ‘sweet spot’, yaw maneuvers were performed uniformly as shown in Fig. 5 with its orbit numbers. The NOAA-20 SDSM Sun view sweet spot was defined as the solar elevation angles between -1.6 and 1.6 degrees and azimuth angles between -18 and 18 degrees. Even though the maximum sweet spot of solar

azimuth angle was defined to be 18 degrees, it didn’t go beyond 0 azimuth during the two years of on-orbit operations

The yaw derived BRDF functions through the RTA and SDSM SD view port were very similar to the prelaunch LUTs within ± 0.04 percent levels in different bands and detectors. But the SDSM Sun transmittance function (τ_{SDSM}) showed significant differences at more than ± 1 percent levels, which caused significant H-factor oscillations. Initially, the τ_{SDSM} function was re-derived by using the yaw data set. Using (3), a new version of H-factors were recalculated along with the newly updated $\tau_{sds} \cdot BRDF_{SDSM}$ LUT. The SDSM detector dependent degradation patterns were restored but the oscillation problem was improved although not completely removed even after applying the yaw maneuver data. To mitigate this H-factor oscillation pattern, NOAA VIIRS SDR team considered to add on-orbit SDSM data sets between the yaw maneuver data sets as shown in Fig. 6. All the on-orbit SDSM operations covered the sweet spot elevation range continuously and the azimuth angles were seasonally and slowly changed in relation with the Sun locations to the SDSM Sun screen. As expected, the yaw maneuver range well covers the on-orbit operational azimuth range that are shown as green vertical lines in Fig. 6. After adding the on-orbit SDSM data, the H-factor oscillation problem was significantly improved to within 0.3% levels in all the SDSM detectors in Fig. 7. Compared to the H-factors using the prelaunch LUTs in Fig. 4, the yaw and on-orbit SDSM data updated H-factors significantly improved the oscillation patterns and showed expected direction of the SD degradations over time with the detector dependencies. In addition, the yaw maneuver points near day 69 in Fig. 7 were tightly clustered together which validated our yaw maneuver analysis and LUT derivations. It also should be noted that the update H-factors were normalized to the day zero point by extrapolating the fits in all the SDSM detectors. The day zero point is defined as the NOAA-20 orbit insertion time on November 18, 2017 at 10:45:08 UTC. We assume that the rate of SD degradation had been constant before the VIIRS activation time (without the on-

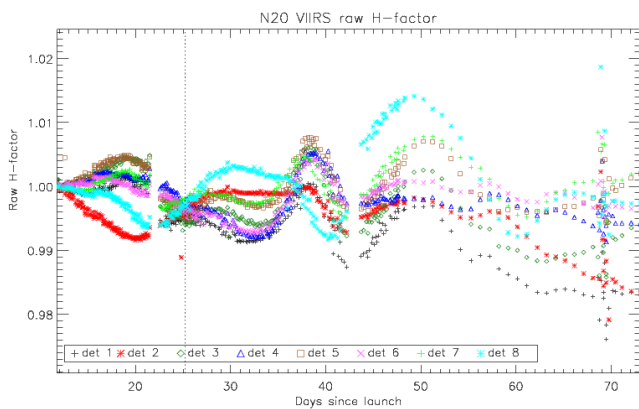


Fig. 4. Initial NOAA-20 VIIRS H-factor using prelaunch LUTs.

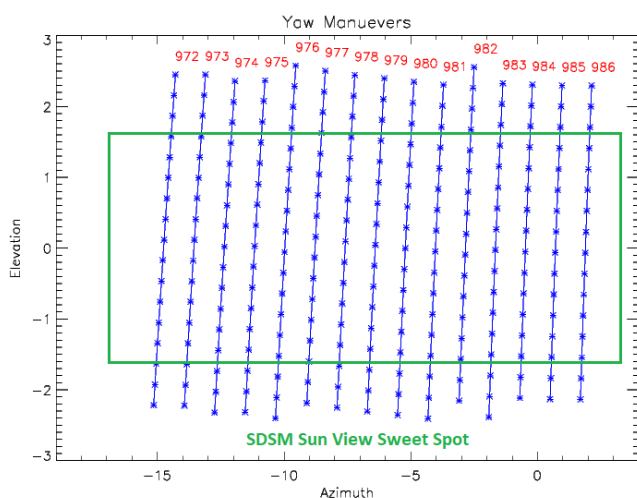


Fig. 5. NOAA-20 VIIRS yaw maneuver coverage in terms of SDSM Sun view elevation and azimuth angles with the sweet spot range. The numbers represent orbit numbers for all the yaw maneuvers.

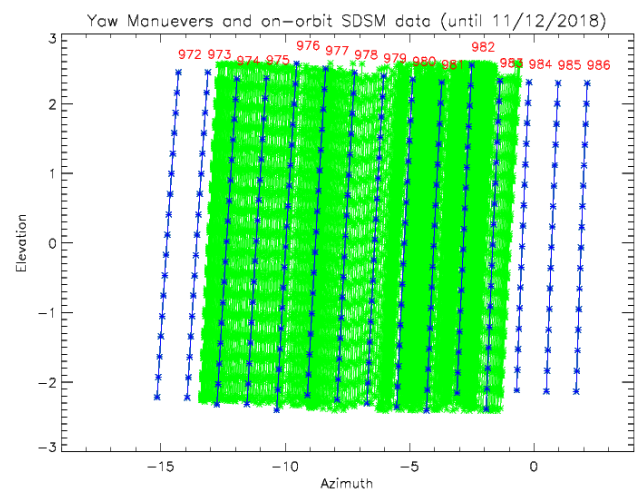


Fig. 6. On-orbit SDSM data is shown in green vertical lines on top of the yaw maneuver data. The on-orbit SDSM data up to orbit number 5100 (until Nov. 12, 2018) lines filled up the gaps between the yaw maneuver lines.

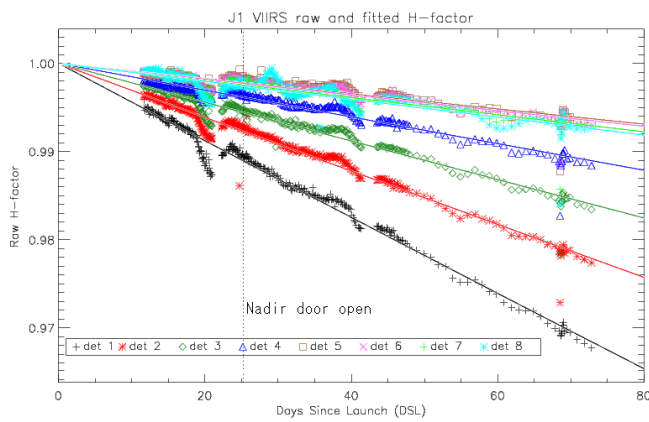


Fig. 7. Initially updated H-factor by using yaw maneuver and on-orbit SDSM data. The dotted line near day 30 indicates the VIIRS EV nadir door open time.

orbit SDSM collections) and it can be extrapolated to the initial point by a function fit in each detector.

Even though the updated τ_{SDSM} LUT reduced oscillations, the detector 6, 7 and 8 H-factors showed abnormally large degradation rates in Fig 7. compared to the S-NPP case [13]. The H-factors with SDSM detector 7 and 8 at wavelengths of 868 and 912 nm had approximately 0.7 percent degradation near the 80 days on-orbit. For S-NPP VIIRS case, this rate was achieved around 5 years of operation. To check this abnormal detector gains, Fig. 8 shows on-orbit SDSM and yaw maneuver data values were plotted at solar elevation angle of 1.0 degrees in SDSM detector 8. The original on-orbit SDSM data sets (red squares) provided detailed structures between the yaw maneuver points (black asterisk) as expected [9]. However, there is a time dependent differences between the yaw and original on-orbit SDSM data points. The differences linearly increased starting from the VIIRS mission with -2 degrees of azimuth angle toward the angle -7 degrees in Fig 8. There was almost no difference between yaw and original on-orbit SDSM data near the azimuth angle of -7 degrees since the yaw maneuvers were performed very close to the on-orbit SDSM data at -7 degrees. It was also assumed that there was no gain

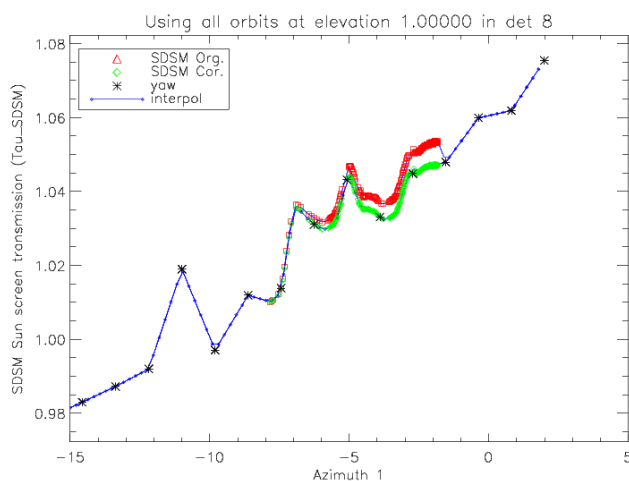


Fig. 8. On-orbit SDSM and yaw maneuver data time dependent gain correction. For better visualization, on-orbit SDSM data sets were selected from the start of the VIIRS activation to orbit number 1034 (until January 30, 2018), which was close to the yaw maneuver date.

changes in either SDSM detectors or VIIRS detectors within one day of yaw maneuver operations. But for the on-orbit SDSM data near -2.5 degrees, there was approximately 2-month time difference which caused time-dependent gain differences ($\sim 0.4\%$). In each solar elevation angle sampling point, the time dependent SDSM detector gains were linearly corrected using the difference between the original on-orbit SDSM and yaw maneuver data sets. The corrected on-orbit SDSM profile is shown as green diamonds in Fig 8. After applying the SDSM detector gain corrections in all the detectors, the corrected on-orbit SDSM and yaw maneuver data sets were aligned properly in the figure.

C. H-factor and F-factor updates

Once the SDSM detector dependency correction was applied, a new version of the τ_{SDSM} LUT was derived and applied to the H-factor equation (3) with a full on-orbit operational range. The updated H-factors are shown in Fig. 9 as of October 9, 2019. Initially, the on-orbit SDSM collections was performed in every orbit and it was reduced to every other orbit on December 8, 2017 (Days Since Launch (DSL) 20). Because there was no problem with its operations, the frequency was reduced to daily starting from January 5, 2018. Later on as shown in Fig 9 in the middle of H-factors, it was further reduced to weekly on Mondays starting from March 1, 2018. The SDSM BRDF LUT was updated only using the yaw maneuver results, since there was no large differences between the prelaunch version and yaw updated LUT. It should be noted that the H-factor in SDSM detector 6, 7, and 8 had been back to normal level after the SDSM gain corrections. The yaw maneuver points were also nicely clustered around day 69 as expected. The H-factor oscillation patterns were improved compared to the initial H-factors in Fig 4.

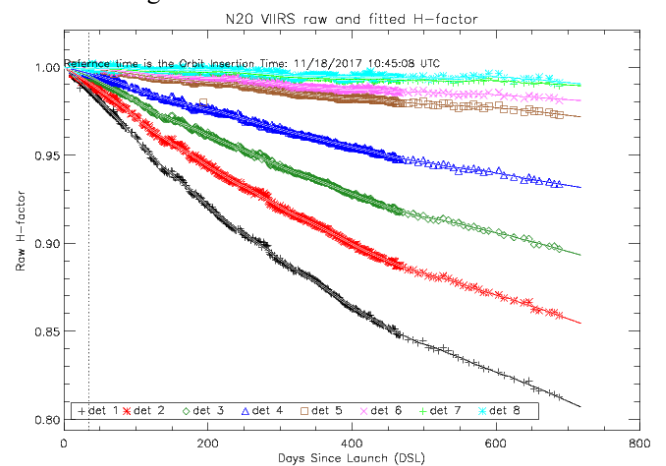


Fig. 9. Updated H-factors using yaw and on-orbit SDSM data sets with SDSM detector gain correction as of October 9, 2019. The collection frequency was changed from daily to weekly on March 1, 2019.

When a stable and reasonable H-factor was ready, the F-factor was derived based on (2) as shown in Fig. 10. The center wavelength differences between the SDSM and VIIRS bands were linearly interpolated in the wavelength domain. The starting points of the VIS/NIR wavelength bands (M1~M7) were less than unity as shown in Fig. 10, which means that there were discrepancies between the theoretical calculated radiance

(nominator) and observed SD radiance (denominator) parts in the SD F-factor equation (2). This indicated possible prelaunch calibration self-deviations which is still under investigation by prelaunch calibration team. On the other hand, the S-NPP SD F-factors were very close to the unity in most of the RSB bands [22].

The F-factors were very stable especially in all RSB bands mostly within one percent level except band M1. Band M1, the shortest wavelength, showed approximately 1.5% detector F-factor decrease (or VIIRS detector gain increase) near DSL 690. Similar F-factor drops (or gain increases) were observed in S-NPP VIIRS case within bands M2~M4 approximately after 2 years of operations [22]. These SD based F-factor decreasing patterns are observed in most of the H-factor applied bands (M1~M7) and these changes need to be validated with lunar F-factors and other trends such as DCC, SNO, and cross calibration results.

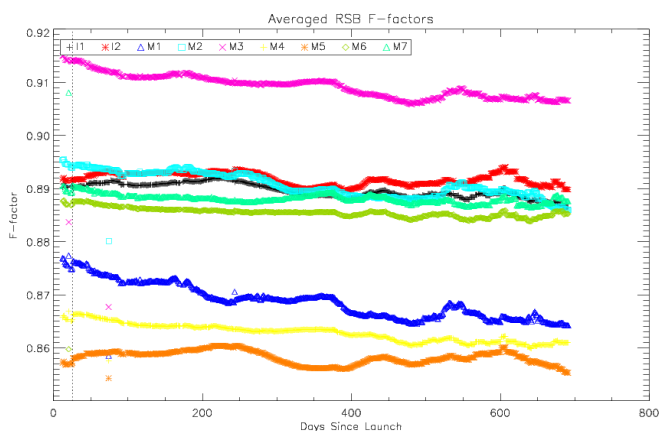


Fig. 10. NOAA-20 VIIRS SD F-factors in VIS/NIR bands.

D. Lunar F-factor Results

The scheduled lunar collections starts with the predictions of chances to view the moon in the SV with the desired lunar phase angle (-51 degrees) and spacecraft roll maneuver. The negative value of the desired phase angle means the moon is in the waxing phase. Usually there are several chance of the lunar collections and NOAA VIIRS team calculates the time and roll angles and validates the collection information with NASA VIIRS team. When reached agreement of the plan, the lunar collection information is notified to the mission operation team. After the lunar collection, the corresponding Raw Data Record (RDR) granules near the collection time are processed to extract the moon image as shown in Fig. 11. All the scheduled lunar collections are listed in Table III. Note that the normal VIIRS SDR products are masked with a fill values in the EV values during the roll maneuver.

To be able to compare the SD and lunar F-factors, lunar F-factors are normalized to the SD F-factors first in each band individually. Then the SD F-factors are also normalized to visualize the percent changes as shown in Fig. 12. The GIRO (or ROLO) lunar irradiance model only can be used for relative calibration changes, since there was high uncertainties of the atmospheric correction and the reverence Vega star irradiance

TABLE III
NOAA-20 VIIRS scheduled lunar collections

| Date | Time [UTC] | Lunar phase angle |
|-------------|------------|-------------------|
| 2017-12-29* | 10:03:56 | -50.58 |
| 2018-1-27 | 19:22:49 | -51.34 |
| 2018-2-26 | 04:47:03 | -51.13 |
| 2018-3-27 | 12:32:59 | -51.16 |
| 2018-4-25 | 20:21:36 | -50.98 |
| 2018-5-25 | 05:53:34 | -50.31 |
| 2018-6-23# | 13:43:07 | -51.42 |
| 2018-11-19 | 01:54:45 | -50.99 |
| 2018-12-18 | 17:56:39 | -51.32 |
| 2019-1-17 | 09:59:05 | -50.81 |
| 2019-2-15 | 22:44:41 | -50.84 |
| 2019-3-17# | 08:11:05 | -51.19 |
| 2019-4-15 | 15:59:10 | -51.02 |
| 2019-05-14 | 22:08:01 | -50.91 |
| 2019-06-13 | 04:17:20 | -50.87 |

*Moon center was located in the 2-sample aggregation zone.

#No lunar roll maneuver was performed.

values. In addition, the GIRO used Wehrli solar irradiance model, whereas NOAA-20 VIIRS uses Thuillier solar model [23]. These solar irradiance model differences may produce different constant levels in the VIIRS RSBs.

In Fig. 11, all the SD F-factors were normalized to the first point of the SD F-factor in each band. Corresponding lunar F-factors were normalized to the second lunar collection because the Cryoradiator door was closed with the first collection which created thermal instability. Note that there were large annual gaps in the lunar F-factors around 300 and 650 DSL because the moon went below the Earth limb during the summer seasons (usually July to October in each year). The long-term trends between SD and lunar F-factors were consistently within one percent level in each band, however, the lunar F-factors showed larger annual oscillation patterns compared to the SD F-factors. With presence of these annual oscillation patterns in both SD and lunar F-factors, the SD F-factors had been decreasing especially in the short wavelength bands of M1 to M4. In band M1 (black solid line in Fig. 11) which showed largest drop approximately 1.5 percent around 700 DSL, the lunar F-factors (black plus signs) did not show the same level of change even though the large annual oscillation was considered. Lunar F-factors even showed stable responses when the same month of the year F-factors were compared based on the information from Table III.

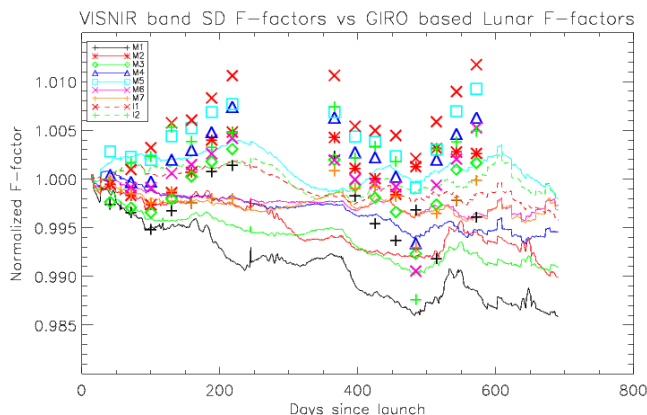


Fig. 11. Normalized SD and lunar F-factors in VIS/NIR bands.

E. DCC Trending Results

Fig. 12 shows NOAA-20 daily DCC time series for bands M1-M4 from January 2018 to September 2019. NOAA-20 VIS/NIR band calibration has been generally stable after the latest F-factor update on April 27, 2018, and comparable to S-NPP. Smaller upward trends were observed ($\sim 0.3\%/year$ in M1 and M2 and $0.2\%/year$ in M3-M4), but their magnitudes are similar to uncertainty levels ($\sim \pm 0.25\%$). Trends in bands M5, M7, and I1-I2 are also small ($\sim 0.1-0.2\%$) and similar to their uncertainty levels. Some variations in NOAA-20 and S-NPP DCC reflectance are observed in November, 2018, possibly caused by uncertainties in the calibration parameters and annual cycles in the DCC reflectance. During the early mission, manual F-factor updates do caused abrupt calibration changes in VIS/NIR radiances, especially in M1-M3. Users are strongly encouraged to use operational NOAA-20 RSB data after April 27, 2018.

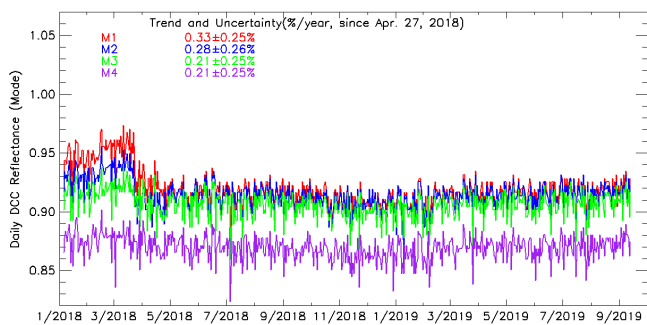


Fig. 12. NOAA-20 bands M1-M4 daily DCC time series. All statistics shown in this figure were calculated using data after the latest F-factor update on April 27, 2018.

F. Cross Calibration Trending Results over SNOs

Fig. 13 shows the bias time series of VIIRS band M1 relative to AQUA MODIS for both NOAA-20 (red) and S-NPP (blue). The difference between the blue and red data indicates the radiometric consistency between the two VIIRS instruments. Although it is expected for two VIIRS instruments to be highly consistent, the study suggests near consistent bias of 2-3% for the entire reflective solar bands. NOAA-20 VIIRS TOA reflectance is lower than S-NPP for all the bands, M1-11. Both SNO (Fig. 13 Top) and SNOx (Fig. 13 Bottom) derived bias time series indicate a large drop in NOAA-20 VIIRS during early launch after applying the on-orbit based H-factor in the operational calibration. Even though the individual VIIRS bias time series is not constant over time, there is no noticeable change in NOAA-20 VIIRS bias relative to S-NPP. This indicates temporally stable NOAA-20 VIIRS calibration relative to S-NPP.

G. Operational F-factor for NOAA VIIRS SDR production

Based on the SD as the primary calibration source, the F-factors derived from the solar measurements have shown a small detector gain increase for the visible and near infrared bands. These changes were not observed in the lunar F-factors as shown in Fig. 11 even though the annual oscillation patterns were considered. On top of the lunar trending results, other long-term DCC, PICS, SNO and SNOx trending results also didn't show any evidence of gain changes especially in the short

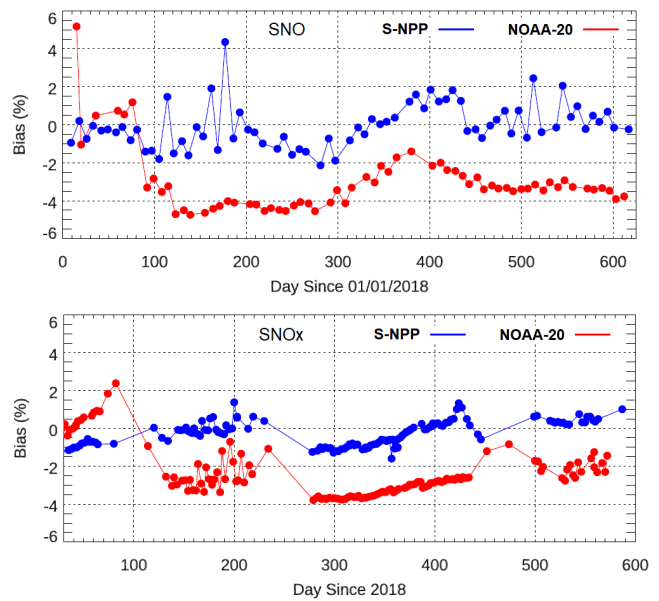


Fig. 13. NOAA-20 VIIRS bias time series using SNO and SNOx for M1. The top figure shows polar snow and the bottom figure shows results from the Saharan desert.

wavelength bands (M1-M4). The near real-time DCC trending and other PICS site trending plots are available on the NOAA Calibration Center (NCC) website at <https://ncc.nesdis.noaa.gov/NOAA-20/VSTS.php>. Fig. 14 shows band averaged NOAA operational F-factors delivered to the VIIRS SDR production system. The initial increases in the F-factors until January 2018 were caused by setting H-factor to be one because of the initial H-factor oscillation problems. That was equivalent to assuming that the observed F factor trends were due to degradation of the VIIRS RSB radiometric response and not due to the SD degradation. However, in hindsight, it is clear that the assumption of response degradation was incorrect. A better approach would have been to extrapolate the F-factor trends to the beginning of the NOAA-20 mission and to use these extrapolated F-factors unchanged until actual H-factor values became available, assuming in effect that the F factor trends were only due to the SD degradation.

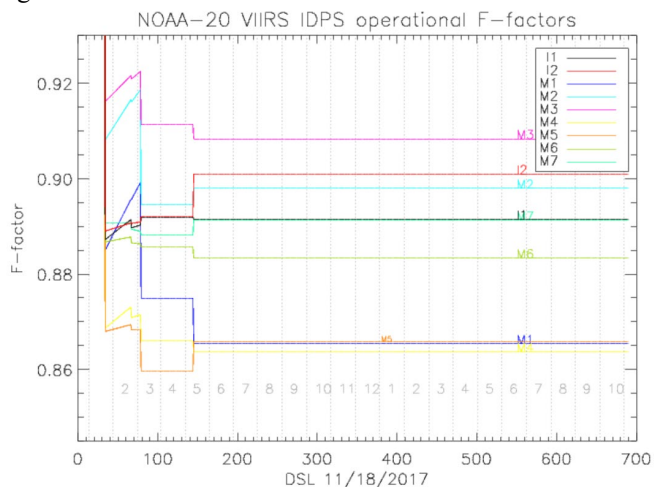


Fig. 14. NOAA-20 VIIRS operational SD F-factors delivered to SDR production as of October 10, 2019.

The actual H-factors were first applied in the F-factor calculations in March 2018 after the processing parameters were improved based on the SDSM measurements during the yaw maneuvers and the regularly scheduled collects. The most satisfactory F-factors were generated only in April 2018 by applying for NOAA-20 the same calibration software, RSBAutoCal, used for Suomi NPP in the NOAA operational processing of VIIRS SDR [24, 25]. These F-factors have been applied in the VIIRS SDR production since April 27, 2018. Based on all the trending results, the RSB F-factors have been maintained constant since then. Nevertheless, NOAA VIIRS team is closely monitoring all these calibration sources to provide best quality of the VIIRS SDR product. Future updates to the RSB F factors can be expected based on further improvements in the processing parameters, including those that may result from the lunar measurements.

V. SUMMARY AND CONCLUSIONS

NOAA-20 VIIRS has been operating normally since its launch on November 18, 2018. The functionalities and performances of the VIIRS sensor were tested and validated through a set of PLTs. This study showed the radiometric calibration related issues, updates and on-orbit validations results in the RSBs.

The primary radiometric source of RSB calibration is based on the SD BRDF with SDS which carried traceability to the prelaunch radiometric calibration standards. Using the SDSM collections, the initial SD degradation results showed abnormal oscillations up to 1.6 percent. To resolve the initial SD degradation anomalies, the combined yaw maneuver data and on-orbit SDSM data set was used to re-derive the $\tau_{sds} \cdot BRDF_{RTA}$, $\tau_{sds} \cdot BRDF_{SDSM}$, and τ_{SDSM} functions. When they were compared to the prelaunch measured LUTs, the τ_{SDSM} function showed significant differences throughout the operational ranges of SDSM elevation and azimuth angles more than 1 percent levels, which directly affected to the SD degradation. With the time-dependent SDSM detector gain correction and updated on-orbit SDSM data set, a stable and reasonable H-factors were achieved and applied to the SD F-factors using RSBAutoCal. As a result, a set of constant

operational F-factors were applied to the NOAA-20 VIIRS SDR production since April 27, 2018.

To monitor the on-orbit detector responsivity changes, the primary radiometric calibration coefficients, the SD F-factors, have been compared with the monthly lunar F-factors. Over the last two years, the lunar F-factors remained mostly in the same level considering annual oscillation patterns. On the other hand, short wavelength SD F-factors in bands M1 to M4 showed F-factor drops approximately 1.5 to 0.5 percent levels. To decide true detector trends, the DCC responses were checked as a part of the post SDR validation. Generally, VIS/NIR band radiometric trends are generally stable after the last operational F-factor update on April 27, 2018. There were small upward trends observed in some bands around 0.3 percent per year levels in M1 and M2 compared to the S-NPP VIIRS results, however, these small changes were less than the uncertainty level of the DCC trends. Another post launch validation was performed by the cross-calibration over the PICS using the Aqua MODIS as a transferring radiometer for S-NPP and NOAA-20 VIIRS sensors. Even though there were large constant bias of two to three presents in all the RSBs, there were no noticeable long-term reflectance ratio changes of NOAA-20 VIIRS bands when compared relatively to the S-NPP VIIRS bands. Considering all the on-orbit calibrations and post SDR product validation results, NOAA VIIRS SDR science team decided to keep the constant operation SD F-factors updated on April 27, 2018 for the best radiometric quality of the NOAA-20 SDR products.

VI. ACKNOWLEDGMENTS

The authors appreciate EUMETSAT for sharing the GIRO lunar irradiance model (version 1.0). This study is funded by the NOAA Joint Polar Satellite System (JPSS) Program with a grant to the University of Maryland. The manuscript contents are solely the opinions of the authors and do not constitute a statement of policy, decision, or position on behalf of NOAA or the U.S. government.

VII. REFERENCES

- [1] T. Choi, S. Blonski, and C. Cao, "Initial on-orbit radiometric calibration of the NOAA-20 VIIRS Reflective Solar Bands," in *SPIE Optical Engineering + Applications*, 2018, vol. 10764, p. 11: SPIE.
- [2] C. Cao, F. J. De Luccia, X. Xiong, R. Wolfe, and F. Weng, "Early On-Orbit Performance of the Visible Infrared Imaging Radiometer Suite Onboard the Suomi National Polar-Orbiting Partnership (S-NPP) Satellite," *IEEE Transactions on Geoscience and Remote Sensing*, vol. 52, no. 2, pp. 1142-1156, 2014.
- [3] C. Cao *et al.*, "NOAA-20 VIIRS on-orbit performance, data quality, and operational Cal/Val support," in *SPIE Asia-Pacific Remote Sensing*, 2018, vol. 10781, p. 9: SPIE.
- [4] C. Cao *et al.*, "Suomi NPP VIIRS sensor data record verification, validation, and long-term performance monitoring," *Journal of Geophysical Research: Atmospheres*, vol. 118, no. 20, pp. 11,664-11,678, 2013.
- [5] C. Cao *et al.*, "NOAA Technical Report NESDIS 142 Visible Infrared Imaging Radiometer Suite (VIIRS) Sensor Data Record (SDR) User's Guide," Sep. 10, 2013 2013.
- [6] J. McIntire, D. Moyer, B. Efremova, H. Oudrari, and X. Xiong, "On-Orbit Characterization of S-NPP VIIRS Transmission Functions," *IEEE Transactions on Geoscience and Remote Sensing*, vol. 53, no. 5, pp. 2354-2365, 2015.
- [7] J. J. Butler, X. Xiong, X. Gu, N. Lei, and X. Xiong, "Product of the SNPP VIIRS SD screen transmittance and the SD BRDF from both yaw maneuver and regular on-orbit data," presented at the Earth Observing Systems XXI, 2016.
- [8] T. Choi, X. Shao, and C. Cao, "On-orbit radiometric calibration of Suomi NPP VIIRS reflective solar bands using the Moon and solar diffuser," *Appl Opt*, vol. 57, no. 32, pp. 9533-9542, Nov 10 2018.
- [9] T. Choi, S. Blonski, X. Shao, and C. Cao, "Improving NOAA 20 VIIRS screen transmittance and solar diffuser BRF estimation from both Yaw maneuver and regular on-orbit data," in *SPIE Remote Sensing*, 2018, vol. 10785, p. 15: SPIE.
- [10] N. Baker and H. Kilcoyne, "Joint Polar Satellite System (JPSS) VIIRS Radiometric Calibration Algorithm Theoretical Basis Document (ATBD)," J. P. S. S. J. G. Project, Ed., ed. NOAA and NASA: NOAA & NASA, 2011.
- [11] X. Shao, C. Cao, and T.-C. Liu, "Spectral Dependent Degradation of the Solar Diffuser on Suomi-NPP VIIRS Due to Surface Roughness-Induced Rayleigh Scattering," *Remote Sensing*, vol. 8, no. 3, 2016.
- [12] D. Moyer, J. McIntire, H. Oudrari, J. McCarthy, X. Xiong, and F. De Luccia, "JPSS-1 VIIRS Pre-Launch Response Versus Scan

- Angle Testing and Performance," *Remote Sensing*, vol. 8, no. 2, 2016.
- [13] T. Choi, X. Shao, C. Cao, and F. Weng, "Radiometric Stability Monitoring of the Suomi NPP Visible Infrared Imaging Radiometer Suite (VIIRS) Reflective Solar Bands Using the Moon," *Remote Sensing*, vol. 8, no. 1, 2015.
- [14] W. Wang and C. Cao, "DCC radiometric sensitivity to spatial resolution, cluster size, and LWIR calibration bias based on VIIRS observations," *Journal of Atmospheric and Oceanic Technology*, vol. 32, no. 1, pp. 48-60, 2015/01/01 2015.
- [15] W. Wang and C. Cao, "Monitoring the NOAA operational VIIRS RSB and DNB calibration stability using monthly and semi-monthly deep convective clouds time series," *Remote Sensing*, vol. 8, no. 1, p. 32, 2016.
- [16] W. Wang, C. Cao, S. Blonski, T. Choi, S. Upreti, and X. Shao, "Evaluation of NOAA-20/S-NPP VIIRS RSB Calibration Performance during Post-Launch Test, Long-term Operational Monitoring, and Reprocessing using Daily Deep Convective Clouds," presented at the 2019 Joint Satellite Conference, Boston, MA, July 28 - August 4, 2019.
- [17] W. Wang and C. Cao, "NOAA-20 VIIRS Sensor Data Records Geometric and Radiometric Calibration Performance One Year In-Orbit," in *2019 International Geoscience and Remote Sensing Symposium (IGARSS)*, Yokohama, Japan, 2019.
- [18] H. Yongxiang, B. A. Wielicki, Y. Ping, P. W. Stackhouse, B. Lin, and D. F. Young, "Application of deep convective cloud albedo observation to satellite-based study of the terrestrial atmosphere: monitoring the stability of spaceborne measurements and assessing absorption anomaly," *IEEE Transactions on Geoscience and Remote Sensing*, vol. 42, no. 11, pp. 2594-2599, 2004.
- [19] C. Cao, M. Weinreb, and H. Xu, "Predicting Simultaneous Nadir Overpasses among Polar-Orbiting Meteorological Satellites for the Intersatellite Calibration of Radiometers," vol. 21, no. 4, pp. 537-542, 2004.
- [20] T. Kimura, X. Xiong, X. Shao, S. Blonski, C. Cao, and S. Upreti, "Assessing the NOAA-20 and S-NPP VIIRS radiometric consistency," presented at the Earth Observing Missions and Sensors: Development, Implementation, and Characterization V, 2018.
- [21] S. Upreti, C. Cao, X. Xiong, S. Blonski, A. Wu, and X. Shao, "Radiometric Intercomparison between Suomi-NPP VIIRS and Aqua MODIS Reflective Solar Bands Using Simultaneous Nadir Overpass in the Low Latitudes," vol. 30, no. 12, pp. 2720-2736, 2013.
- [22] T. Choi and C. Cao, "S-NPP VIIRS On-Orbit Calibration Coefficient Improvements With Yaw Maneuver Reanalysis," *IEEE Transactions on Geoscience and Remote Sensing*, vol. 57, no. 10, pp. 7460-7465, 2019.
- [23] T. Choi, X. Shao, S. Blonski, W. Wang, S. Upreti, and C. Cao, "NOAA-20 VIIRS initial on-orbit radiometric calibration using scheduled lunar observations," presented at the Earth Observing Systems XXIV, 2019.
- [24] K. Rausch, S. Houchin, J. Cardema, G. Moy, E. Haas, and F. J. De Luccia, "Automated calibration of the Suomi National Polar-Orbiting Partnership (S-NPP) Visible Infrared Imaging Radiometer Suite (VIIRS) reflective solar bands," *Journal of Geophysical Research: Atmospheres*, vol. 118, no. 24, pp. 13,434-13,442, 2013.
- [25] S. Blonski and C. Cao, "Suomi NPP VIIRS Reflective Solar Bands Operational Calibration Reprocessing," *Remote Sensing*, vol. 7, no. 12, pp. 16131-16149, 2015.